iScience

CellPress
OPEN ACCESS

Article

Generative pretraining from large-scale transcriptomes for single-cell deciphering

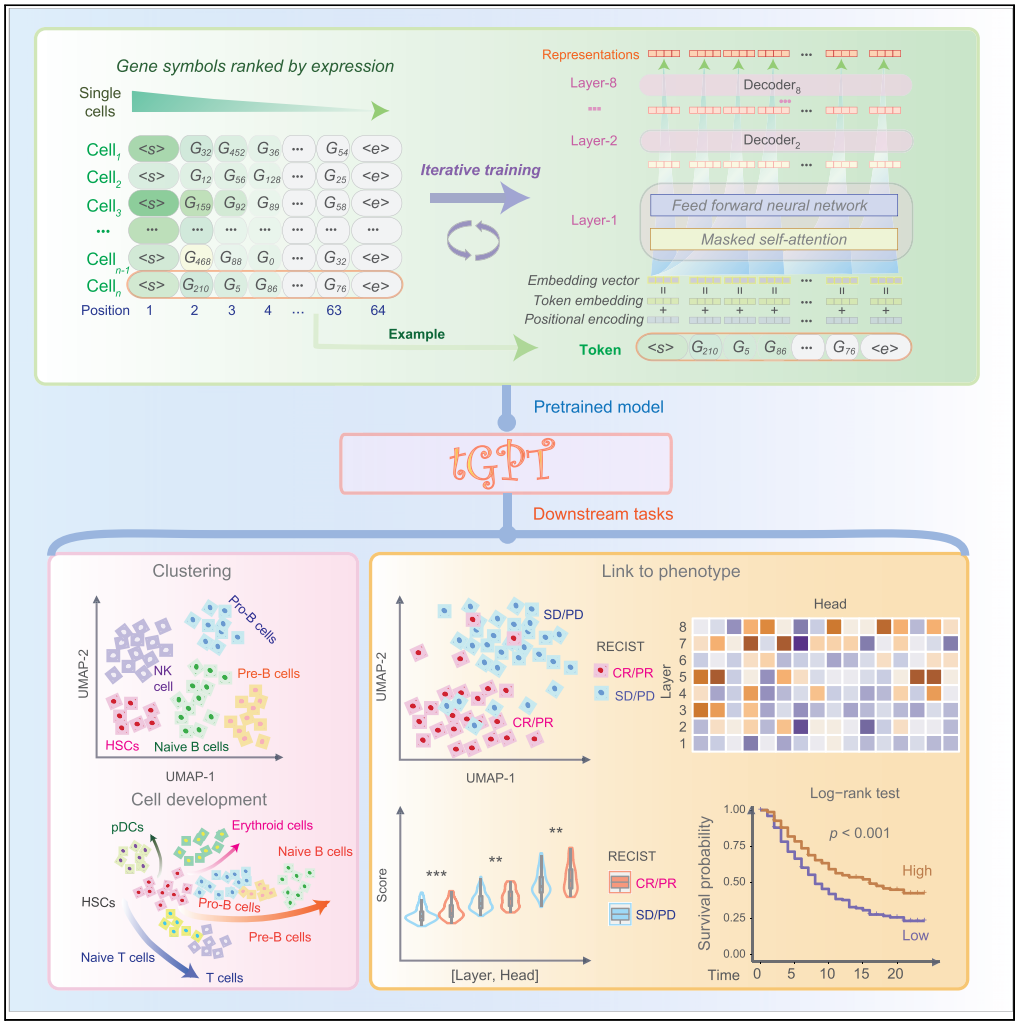

Hongru Shen, Jilei Liu, Jiani Hu, ..., Jilong Yang, Kexin Chen, Xiangchun Li

chenkexin@tmu.edu.cn (K.C.)
lixiangchun2014@foxmail.com (X.L.)

Highlights

tGPT models gene rankings via autoregressive language modeling

tGPT works effectively on fundamental single-cell analysis tasks

tGPT captures distinctive features of different cell types

tGPT learns expression signatures linked to genomic and clinical features

Shen et al., iScience *26*, 106536
May 19, 2023
https://doi.org/10.1016/j.isci.2023.106536

iScience

CellPress
OPEN ACCESS

Article

Generative pretraining from large-scale transcriptomes for single-cell deciphering

Hongru Shen,[1,5] Jilei Liu,[1,5] Jiani Hu,[1,5] Xilin Shen,[1] Chao Zhang,[2] Dan Wu,[1] Mengyao Feng,[1] Meng Yang,[1] Yang Li,[1] Yichen Yang,[1] Wei Wang,[3] Qiang Zhang,[4] Jilong Yang,[2] Kexin Chen,[3,*] and Xiangchun Li[1,6,*]

SUMMARY

Exponential accumulation of single-cell transcriptomes poses great challenge for efficient assimilation. Here, we present an approach entitled generative pretraining from transcriptomes (*tGPT*) for learning feature representation of transcriptomes. *tGPT* is conceptually simple in that it autoregressive models the ranking of a gene in the context of its preceding neighbors. We developed *tGPT* with 22.3 million single-cell transcriptomes and used four single-cell datasets to evaluate its performance on single-cell analysis tasks. In addition, we examine its applications on bulk tissues. The single-cell clusters and cell lineage trajectories derived from *tGPT* are highly aligned with known cell labels and states. The feature patterns of tumor bulk tissues learned by *tGPT* are associated with a wide range of genomic alteration events, prognosis, and treatment outcome of immunotherapy. *tGPT* represents a new analytical paradigm for integrating and deciphering massive amounts of transcriptome data and it will facilitate the interpretation and clinical translation of single-cell transcriptomes.

INTRODUCTION

Rapid advancement in single-cell RNA sequencing leads to dramatic drop in sequencing cost and allows for millions of single-cell transcriptomes to be digitized in a single experiment simultaneously. The whole human body is estimated to have 30 trillion cells. Single-cell transcriptome sequencing provided an unprecedented resolution to distinguish different cell type clusters, depict hierarchical cell arrangement and decipher transitional cell states. To achieve this goal, multiple single-cell atlasing projects have been established internationally, including Human Cell Atlas (HCA),[1] Single Cell Expression Atlas (SCEA),[2] COVID-19 Atlas,[3] Tabula Muris Atlas[4] and Mouse Cell Atlas.[5] The HCA project[1] aims to digitize all cells and create a reference map of the human body through community-driven initiative that researchers all around the world can contribute. SCEA[2] compiles and annotates publicly available single-cell transcriptomes across multiple species and different studies. The COVID-19 Atlas[3] aims at elucidating molecular mechanism and therapeutic target of COVID-19 by generating single-cell atlas of SARS-CoV-2 infection in COVID-19 patients. The Tabula Muris[4] and MCA[5] atlases constitute the single-cell reference maps of mouse with millions of cells obtained from different organs. These atlasing projects pose tremendous challenge in the integration of diverse transcriptomes from different projects. However, single-cell transcriptomes are generated by different platforms and experimental protocols. They are sparse, noise and prone to batch effect.[6,7] Therefore, an analytical method to efficiently integrate ten millions of cells are urgently needed.

Over the past few years, deep learning approaches have led to seismic changes in image recognition and natural language understanding. The success of deep learning could largely attribute to the availability of big data, advancement in computational infrastructure, expressivity and scalability of the computational model. The deep learning model could adeptly handle super large-scale high dimensional data and assimilate real-world information. Owing to the exponential accumulation of millions of cell transcriptomes, elucidation of the reference map of single-cell transcriptomes with deep learning becomes an attractive application. Deep learning methods such as *scVI*,[8] *SAUCIE*[9] and *INSCT*[10] have been developed for the analysis of single-cell transcriptomes.

The progress of artificial intelligence is undergoing a paradigm shift in computer vision and natural language processing. Deep neural networks based on transformer are becoming the *de facto* approach in wide variety of scenarios such as vision, language and reasoning.[11] Transformer-based models pretrained

[1]Tianjin Cancer Institute, Tianjin's Clinical Research Center for Cancer, National Clinical Research Center for Cancer, Tianjin Medical University Cancer Institute and Hospital, Tianjin Medical University, Tianjin, China

[2]Department of Bone and Soft Tissue Tumor, Tianjin's Clinical Research Center for Cancer, National Clinical Research Center for Cancer, Tianjin Medical University Cancer Institute and Hospital, Tianjin Medical University, Tianjin, China

[3]Department of Epidemiology and Biostatistics, Tianjin's Clinical Research Center for Cancer, Key Laboratory of Molecular Cancer Epidemiology of Tianjin, National Clinical Research Center for Cancer, Tianjin Medical University Cancer Institute and Hospital, Tianjin Medical University, Tianjin, China

[4]Department of Maxillofacial and Otorhinolaryngology Oncology, Tianjin's Clinical Research Center for Cancer, National Clinical Research Center for Cancer, Tianjin Medical University Cancer Institute and Hospital, Tianjin Medical University, Tianjin, China

[5]These authors contributed equally

[6]Lead contact

*Correspondence: chenkexin@tmu.edu.cn (K.C.), lixiangchun2014@foxmail.com (X.L.)

https://doi.org/10.1016/j.isci.2023.106536

on broad data at scale continues to achieve state-of-the-art progress in image classification[12,13] and language understanding.[14–16] The success of these pretrained models can be attributed to their high expressivity and scalability enabled by transformer to assimilate feature representation from massive amount of unlabeled data. However, the investigation of single-cell transcriptome pretraining at scale has not been well studied.

In this study, we present a deep learning approach entitled *tGPT* toward integration of unlimited number of cells. *tGPT* is built on transformer that has been widely used in natural language understanding and image recognition. The transformer is an essential component and key success of foundation models because of its high expressivity and scalability.[11] *tGPT* takes as input the expression rankings of top-expressing genes rather than the actual expression levels. Rank-based methods for gene expression have been demonstrated to be insensitive to batch effects and data normalization.[17–20] *tGPT* is conceptually simple and empirically efficient. It models the occurrence of a gene in the context of its preceding neighbors' rankings. We developed *tGPT* with 22.3 million cells and systematically evaluated *tGPT* on four heterogeneous datasets for sensitivity to batch-effect, delineation of clustering performance and inference of developmental lineages. We applied *tGPT* to bulk cancer tissue sequencing samples and found that features obtained from *tGPT* are significantly associated with diverse genomic alteration events, patients' prognosis and treatment outcome of immunotherapy. *tGPT* represents a new analytical paradigm to integrate and decipher large-scale single-cell transcriptomes. It will facilitate the integration and clinical translation of large volume of single-cell transcriptome data.

RESULTS

An overview of *tGPT* and its downstream applications

The analytical framework of *tGPT* (Figure 1) consists of three components: Development of *tGPT*, applications of *tGPT* for single-cell clustering, inference of developmental lineage, and interrogation of feature representation of bulk tissues in relation to genomic alterations, prognosis and treatment response of immunotherapy.

tGPT is formatted as an autoregressive language model in that the output from the previous step is used as input to the next step. The input to *tGPT* is a sequence of gene symbols that are ranked by their expression levels. The purpose is to predict the index of the next gene in the dictionary in the context of all previous genes. The dictionary consists of 20706 protein-coding genes. *tGPT* is trained as an unsupervised generative pretraining task.[16] Specifically, for a given cell, let $\mathcal{G} = \{G_1, G_2, \ldots G_n\}$ denote the gene symbols that are sorted in a descending order according to their expression levels. We use the standard language modeling objective $\mathcal{L}(\mathcal{G}) = \sum_i log\, P(G_i|G_{i-k}, \ldots, G_{i-1}; \boldsymbol{\theta})$ to maximize the likelihood. Here, k is the width of context window and $\boldsymbol{\theta}$ are the parameters of *tGPT* that is used to model the conditional probability. The neural network consists of 8 transformer decoder blocks[21] with 1024 hidden units and 16 attention heads.

Quantitative evaluations of *tGPT* on clustering

We systematically evaluated the clustering performance of *tGPT* on four heterogeneous single-cell datasets of different sizes (50-586k cells) from different species and two bulk tissue sequencing datasets (Tables S1 and S2). These four single-cell datasets include Human Cell Atlas Census of Immune Cells[22] (*HCA*, n = 282,558), Human Cell Landscape[23] (*HCL*, n = 586,135), *Tabula Muris*[4] (n = 54,862) and *Macaque Retina*[24] (n = 124,965) dataset (See STAR Methods for description). The two bulk tissue datasets are *Genotype-Tissue Expression*[25] (*GTEx*, n = 11,688) derived from 30 organs and *The Cancer Genome Atlas*[26] (*TCGA*, n = 9,318) consisted of 33 cancer types.

We observed that *tGPT* is insensitive to batch effect as benchmarked against with the other methods that support batch-correction such as *ComBat*,[27] *MNN*,[28] *Harmony*,[29] *Seurat*,[30,31] *BBKNN*,[32] *Scanorama*,[33] *Pegasus*,[34] *scVI*,[8] *scArches*,[35] *iMAP*[36] and *DESC*[37] as measured on the *HCA* dataset. *tGPT* achieved a comparable *kBET* acceptance rate[38] of 0.87 among the aforementioned batch-correction methods (Figure S1L). The UMAP plots of these batch-correction methods and their clustering metrics and grid-search results are provided in Figures S1A–S1K, 2, and 3, respectively.

The clustering performance of *tGPT* is robust with respect to the numbers of top-expression genes being used. We found that the performance of *tGPT* pretrained on the ranking of top 62 and 126 genes were comparable across these six datasets (Figure S4). In addition, we observed that clustering performance on

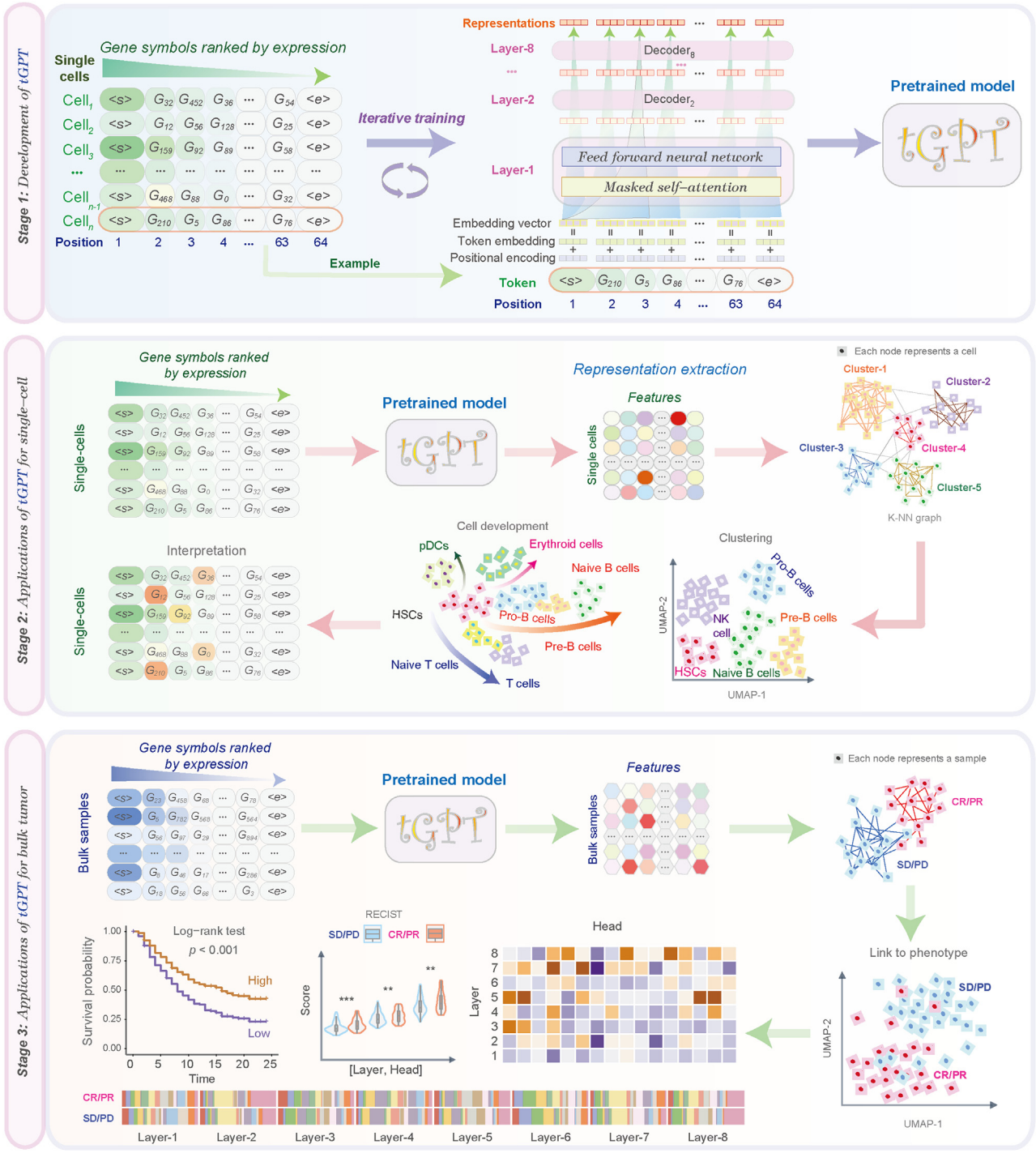

Figure 1. A flowchart illustrating the framework of *tGPT* and its downstream applications

It consists of three components: development of *tGPT*, applications of *tGPT* for single-cell and bulk tissue transcriptomes.

features extracted from different transformer layers [Layer-1, …, Layer-8] are comparable and better than features extracted from the embedding layer across all these six datasets (Figure S4). For each method, we reported the best performance via grid-search to identify optimal values of two parameters that are most relevant to clustering (see STAR Methods). The results from grid-search were provided in Figures S5–S10 and Data S1. Quantitatively, *tGPT* achieved an *Normalized Mutual information* (*NMI*) ranged from 0.75 on

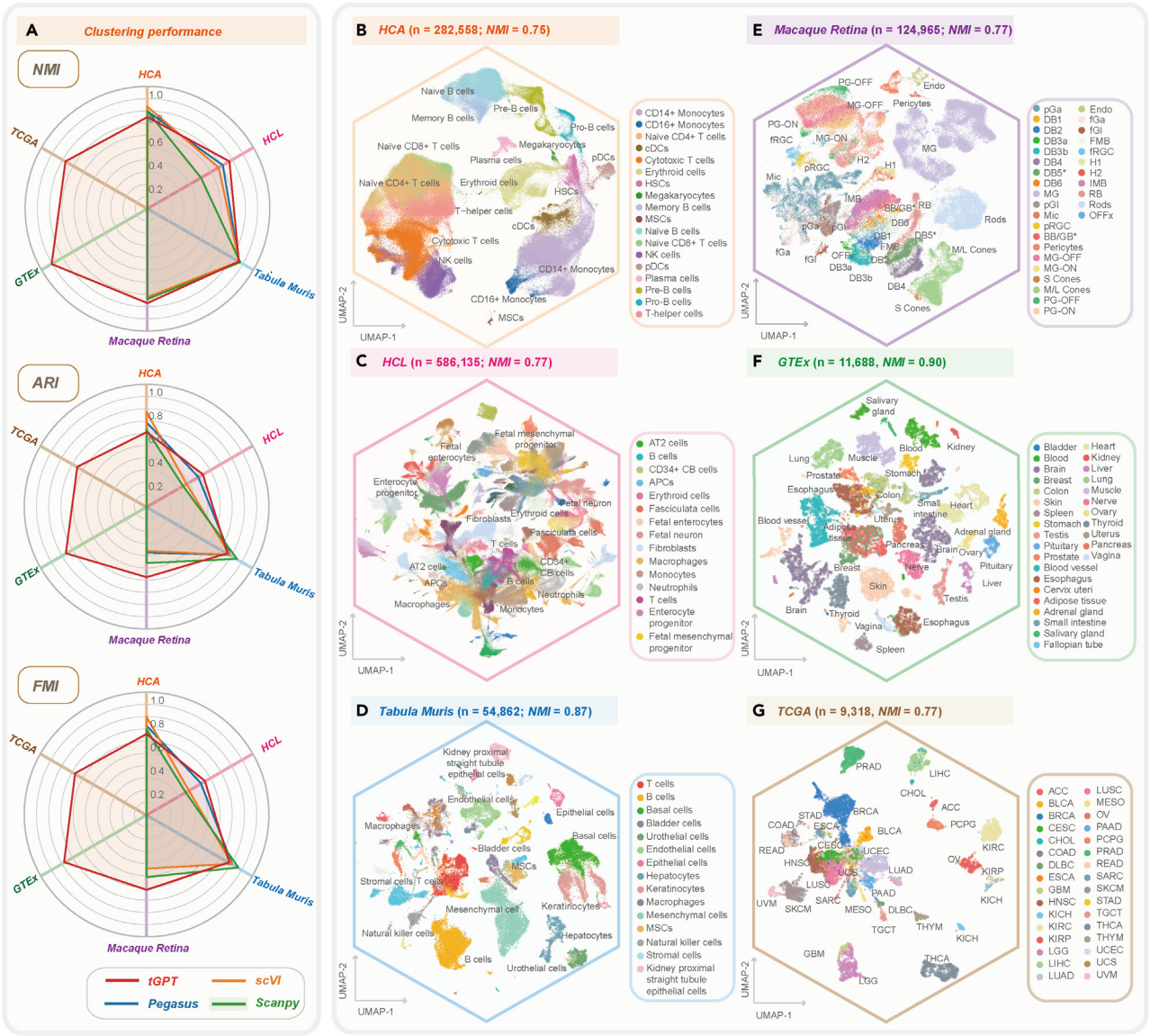

Figure 2. The clustering performance of *tGPT* on four single-cell and two bulk tissue datasets

(A) Radar charts depicting clustering metrics of *tGPT*, *Pegaus*, *scVI* and *Scanpy* across these six datasets.

(B–G) UMAP visualization of feature representations learned by *tGPT* on the *HCA* (B), *HCL* (C), *Tabula Muris* (D), *Macque Retina* (E), *GTEx* (F) and *TCGA* (G).*NMI*, Normalized Mutual information; *ARI*, Adjusted Rand Index; *FMI*, Fowlkes-Mallows Index.

HCA to 0.90 on *GTEx*, *Adjusted Rand Index* (*ARI*) from 0.53 on *HCL* to 0.84 on *Tabula Muris* and *Fowlkes-Mallows Index* (*FMI*) from 0.55 on *HCL* to 0.85 on *Tabula Muris* (Figure 2A). The clustering performance achieved by *tGPT* are comparable to the other methods such as *Scanpy*,[39] *Pegasus*[34] and *scVI*[8] (Figures 2A and S11–S13). Grid-search results of these methods were provided in Figure S14. Running time of these methods were provided in Table S3.

Across these datasets, *tGPT* was capable of grouping cells with the same or similar types (Figures 2B–2G). On the *HCA* dataset, *tGPT* was able to identify cells at different developmental phases. For example, it can delineate B cells of different types such as naive B cells, precursor B (pre-B) cells and progenitor B (pro-B) cells and homologous cells, such as conventional DCs (cDCs) and plasmacytoid DCs (pDC), $CD14^{+}$ and $CD16^{+}$ monocytes. Less represented cell types such as megakaryocytes (0.32%) and MSCs (0.10%) were also captured by *tGPT* (Figure 2B). On the *HCL* dataset, *tGPT* was able to distinguish between immune cells

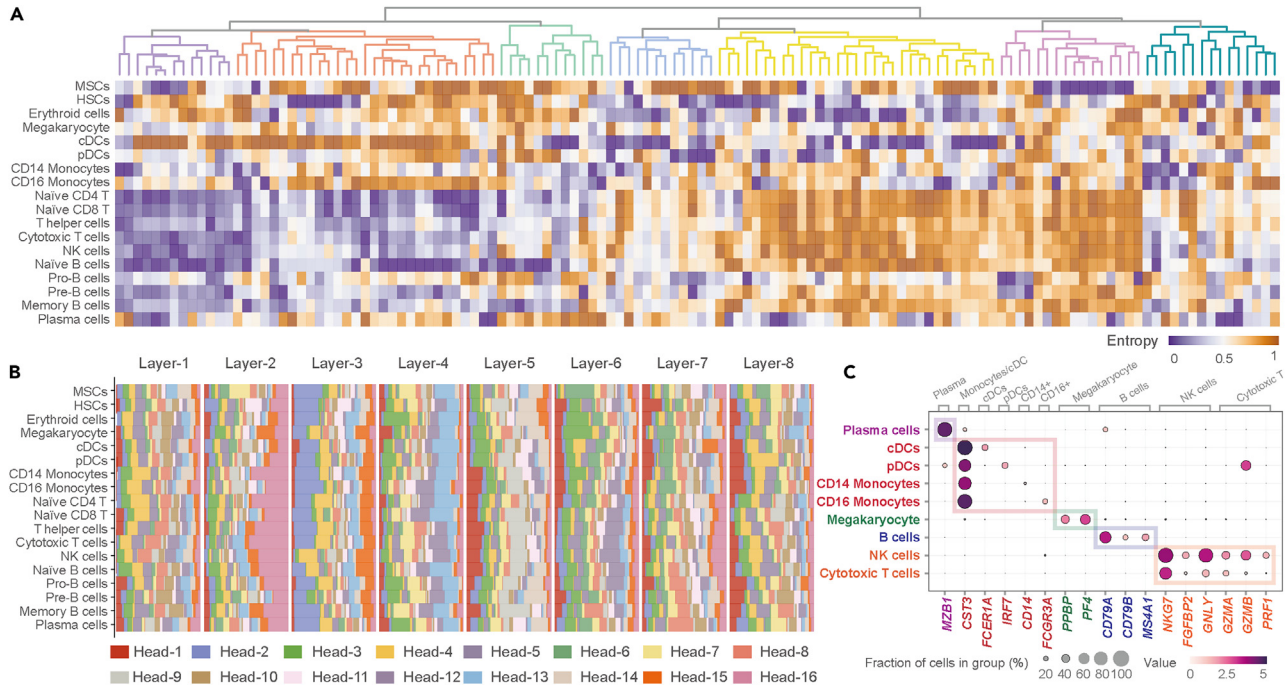

Figure 3. Distinct features of different cell types from the *HCA* dataset learned by *tGPT*

(A) Heatmap representation of attention head entropy for different cell types, and hierarchical clustering plot clustered these attention heads.

(B) Heatmap representation of attention head importance for different cell types.

(C) Dot plot illustrating the attribution scores for cell type specific genes, gray cell types annotated the clusters of marker genes.

and nonimmune cells as well as different cell types from fetus and adult such as fetal enterocytes and adult enterocytes (Figures 2C and S12). On the *Tabula Muris* dataset, *tGPT* was also able to delineate 55 distinct cell types originated from 20 mouse organs (Figures 2D and S13). On the *Macaque Retina* dataset, distinctive cell clusters from foveal and peripheral regions of fascicularis retina defined by *tGPT* are well matched with cell types defined in the original literature[24] (Figure 2E). On the *GTEx* dataset, *tGPT* is able to identify different tissues originated from lineage of organs (*NMI* = 0.90), and samples with similar histological structure are close together such as colon, small intestine and stomach (Figure 2F). On the *TCGA* dataset, different cancer types are well separated (*NMI* = 0.77). Cancer types with the same tissue of origin tend to clump together in the feature representation spaces captured by *tGPT*. For example, adenocarcinomas and squamous cell carcinomas are closely related in the UMAP plots, respectively. Different cancer subtypes originated from the same tissues are well separated such as lung cancer subtypes (e.g., LUAD and LUSC; Figure 2G), kidney cancer subtypes (e.g., KIRC, KIRP and KICH; Figure 2G) and breast cancer subtypes (e.g., Luminal A, Luminal B, HER+ and Basal cell carcinoma; Figure S15). In addition, tGPT achieved *Bilingual Evaluation Understudy* (*BLEU*) scores $\geq$0.69 four datasets examined in this study (Table S4). This suggested that tGPT obtained good quality in gene ranking generation.

Distinct features learned by *tGPT* are connected to cell types

We observed that the head entropy and importance of different cell types from the *HCA* dataset (See STAR Methods) are distinctive from each other. Cells of similar lineages or functions such as T-lineage cells exhibited similar entropy patterns (Figure 3A). The head importance is varying considerably for different cell types, however, cells of similar types are alike as compared with the other cell types (Figure 3B). For each cell type, we calculated the contribution of each gene on the cell final feature representation (See STAR Methods). Celltype specific genes have higher attribution scores (Figure 3C). For example, *NKG7*, *FGFBP2*, *PRF1*, *GNLY*, *GZMA* and *GZMB* are highly represented in cytotoxic T cells and NK cells (Figure S16A). *PPBP* and *PF4* are also highly represented in megakaryocytes (Figure S16B). B-lineage cells have high attribution scores for both *CD79A* and *CD79B*. Attribution scores of *MS4A1* and *MZB1* are relative higher in memory B cells and plasma cells, respectively (Figure S16C). The attribution score of *CST3* is higher among $CD14^+$ monocytes, $CD16^+$ monocytes, cDCs and pDCs. In addition, each specific cell types can be defined by specific genes with high attribution scores, for

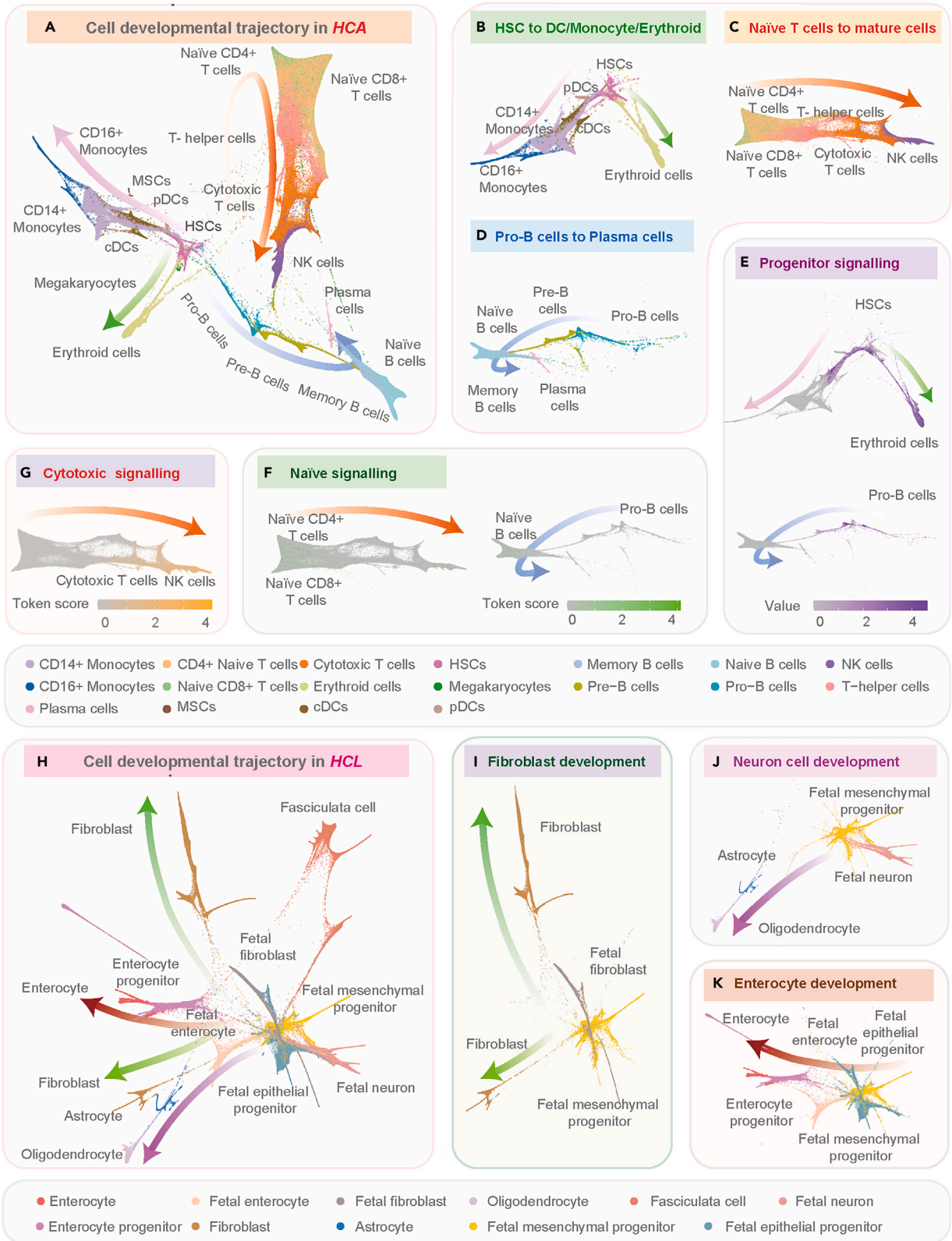
A Cell developmental trajectory in HCA
Naïve CD4+ T cells
Naïve CD8+ T cells
CD16+ Monocytes
T- helper cells
MSCs
pDCs
Cytotoxic T cells
CD14+ Monocytes
HSCs
cDCs
NK cells
Megakaryocytes
Plasma cells
Pro-B cells
Naïve B cells
Erythroid cells
Pre-B cells
Memory B cells
B HSC to DC/Monocyte/Erythroid
HSCs
pDCs
CD14+ Monocytes
cDCs
CD16+ Monocytes
Erythroid cells
C Naïve T cells to mature cells
Naïve CD4+ T cells
T- helper cells
Naïve CD8+ T cells
Cytotoxic T cells
NK cells
D Pro-B cells to Plasma cells
Naïve B cells
Pre-B cells
Pro-B cells
Memory B cells
Plasma cells
E Progenitor signalling
HSCs
Erythroid cells
Pro-B cells
Value
0
2
4
G Cytotoxic signalling
Cytotoxic T cells
NK cells
Token score
0
2
4
F Naïve signalling
Naïve CD4+ T cells
Naïve CD8+ T cells
Naïve B cells
Pro-B cells
Token score
0
2
4
CD14+ Monocytes
CD4+ Naive T cells
Cytotoxic T cells
HSCs
Memory B cells
Naive B cells
NK cells
CD16+ Monocytes
Naive CD8+ T cells
Erythroid cells
Megakaryocytes
Pre−B cells
Pro−B cells
T−helper cells
Plasma cells
MSCs
cDCs
pDCs
H Cell developmental trajectory in HCL
Fibroblast
Fasciculata cell
Fetal fibroblast
Enterocyte progenitor
Enterocyte
Fetal mesenchymal progenitor
Fetal enterocyte
Fibroblast
Fetal epithelial progenitor
Fetal neuron
Astrocyte
Oligodendrocyte
I Fibroblast development
Fibroblast
Fetal fibroblast
Fibroblast
Fetal mesenchymal progenitor
J Neuron cell development
Fetal mesenchymal progenitor
Astrocyte
Fetal neuron
Oligodendrocyte
K Enterocyte development
Enterocyte
Fetal enterocyte
Fetal epithelial progenitor
Enterocyte progenitor
Fetal mesenchymal progenitor
Enterocyte
Fetal enterocyte
Fetal fibroblast
Oligodendrocyte
Fasciculata cell
Fetal neuron
Enterocyte progenitor
Fibroblast
Astrocyte
Fetal mesenchymal progenitor
Fetal epithelial progenitor

Figure 4. Diffusion pseudo-time analysis on the *HCA* and *HCL* datasets

(A) The diffusion map of *HCA* dataset.

(B) Hematopoietic stem cells (HSCs) to erythroid cells or dendritic cells (DCs) and monocytes.

(C) Naive T cells to cytotoxic T cells and nature killer (NK) cells.

(D) Pro-B cells to plasma cells.

(E–G) Cell state signatures for progenitor signaling, naive signaling and cytotoxic signaling.

(H–K) The diffusion map of *HCL* dataset and its main branches. Token score is the norm of the learned token features extracted from *tGPT*.

instance plasmacytoid dendritic cells (pDCs, *IRF7*), conventional dendritic cells (cDC, *FCER1A*), $CD14^+$ monocytes (*CD14*) and $CD14^+$ monocytes (*FCGR3A*) (Figure S16D).

Inference of developmental lineage

We used the feature representations learned by *tGPT* to construct cell pseudo-temporal trajectories on *HCA* and *HCL* datasets (See STAR Methods). On the *HCA* dataset, the developmental trajectories originated from stem cells and differentiated toward multiple biologically functional cell branches (Figure 4A): HSCs to erythroid cells[40] or DCs and monocytes (Figure 4B); naive T cells to cytotoxic T cells and NK cells[41] (Figure 4C); pro-B cells to pre-B cells, then followed by matured naive B cells, and finally bifurcated into memory B cells or plasma cells[42] (Figure 4D). In addition, we observed that the cell state signatures are aligned with cell developmental lineages (See STAR Methods). For instance, HSCs and pro-B cells are manifested by apparent progenitor signaling (Figure 4E). Naive and mature T cells are featured by distinguishable patterns (Figures 4F and 4G).

On the *HCL* dataset, the developmental tree depicted three differential trajectories of fetal mesenchymal progenitor cells into different mature cell types (Figure 4H) with fetal cells at the center of the landscape. The fetal mesenchymal progenitor cells are differentiated into biologically functional fibroblasts (Figure 4I), enterocytes (Figure 4J), astrocytes and oligodendrocytes (Figure 4K).

Clinical significance of *tGPT* in bulk sequencing sample

Here, we demonstrated that *tGPT* is able to capture clinically significant patterns. On the *TCGA* dataset, we found that the importance scores are varying considerably for different attention heads among different layers. The importance score patterns can cluster different cancer types into distinct groups in that cancer of the same tissue-of-origin are closely related whereas cancers of different origins are well separated (See STAR Methods, Figure 5A). For example, skin cutaneous melanoma (SKCM) and uveal melanoma (UVM), glioblastoma multiforme (GBM) and brain lower grade glioma (LGG) are respectively located in the same clustering branches. In addition, we examined the association between attention head entropy and molecular alteration events (See STAR Methods). There are several attention heads exhibited significant association with tumor mutation burden (TMB) in the TCGA pan-cancer cohort and specifically in bladder urothelial carcinoma (BLCA), LUAD and LUSC (Figure 5B). We observed that attention heads also showed significant association with *TP53* mutations at the pan-cancer level and across 9 cancer types (Figure 5C). There are also attention heads exhibited significant association with homologous recombination deficiency (HRD) and genome doubling (Figures 5D and 5E) at the pan-cancer level. The association of attention heads with HRD and genome doubling are statistically significant across 4 and 14 cancer types, respectively. Meanwhile, the attention heads exhibited prognostic significance at pan-cancer level (Figure 5E) and across 7 cancer types (Figure S17).

In addition, we examined the attention head patterns in relation to immunotherapy in an immune checkpoint block (ICB) clinical trial of urothelial carcinoma consisted of 298 patients: 25 patients with CR, 43 with PR, 63 with SD and 63 with PD (See STAR Methods). We found that importance and entropy scores are distinguishable amongst patients with different therapeutic outcome (Figures 5G and 5H). We observed gradually varying entropy values from SD to PR to CR by taking the PD baseline (Figure 5I) and significant difference among 5 attention heads in patients with CR/PR versus SD/PD (Figure 5J). We quantified expression signatures such as tumor evasion and T cell immune infiltration attended by different attention heads (See STAR Methods). By taking PD as baseline, we observed a gradually decreasing patterns of tumor evasion and increasing patterns of T cell immune infiltration from SD to PR to CR (Figures 5K and 5L). The attention heads also exhibited prognostic significance in this clinical trial (Figures 5M and 5N).

DISCUSSION

Efficient integration of accumulating large-scale single-cell transcriptomes is urgently needed. Here, we introduced a conceptually simple approach toward the integration of unlimited number of single-cell

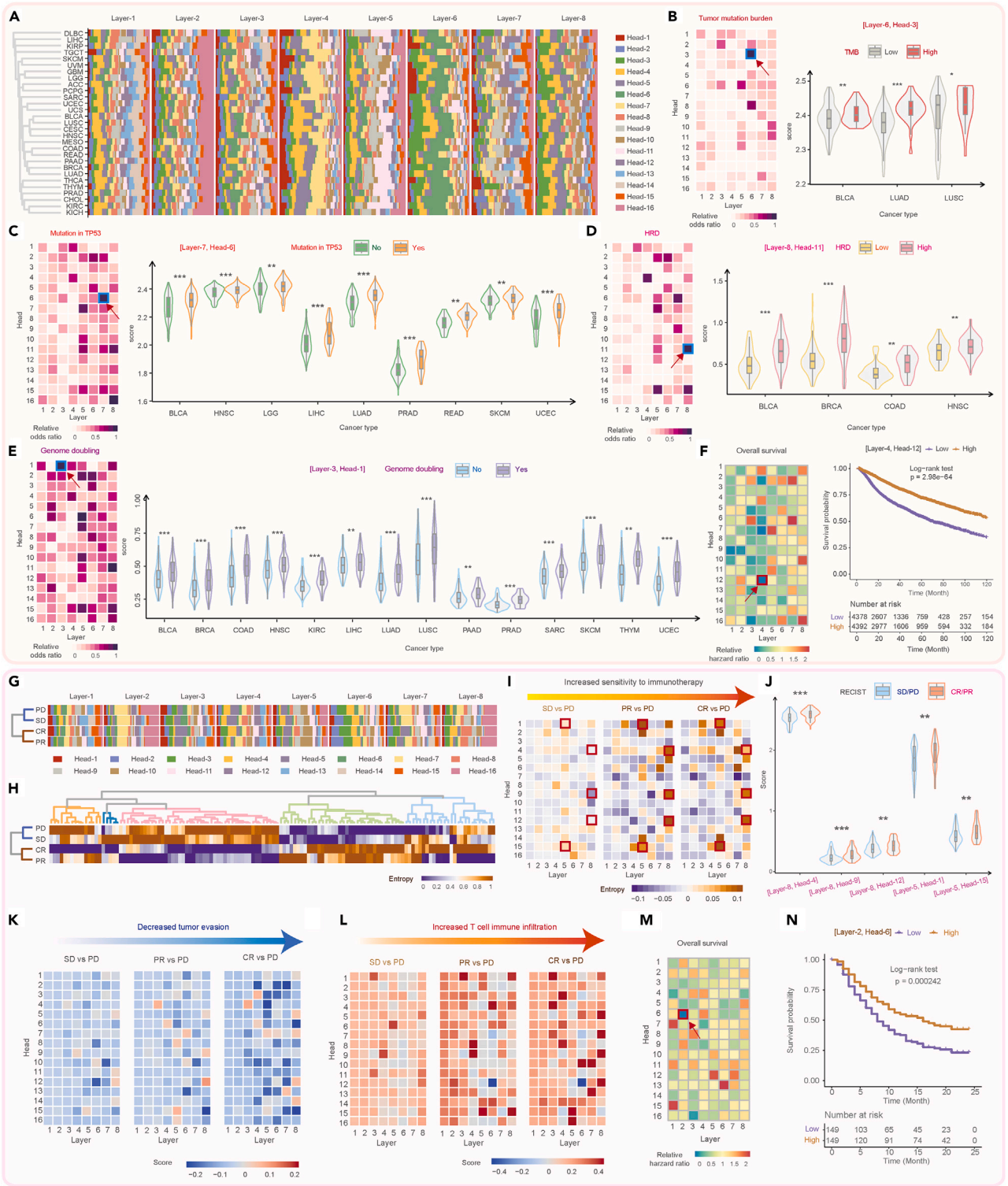

Figure 5. The association of features learned by *tGPT* versus genomic alteration events and clinical phenotype

(A) Heatmap representation of attention head importance score across different cancer types on the *TCGA* dataset.

(B–F) Association of attention head entropy versus tumor mutation burden (B), *TP53* mutation (C), homologous recombination deficiency (D), genome doubling (E) and overall survival (F) on the TCGA cohort.

(G and H) Heatmap representation of attention head importance and entropy on the urothelial carcinoma stratified by RECIST response. CR, complete response; PR, partial response; SD, stable disease; PD, progress disease.

Figure 5. *Continued*
(I) The varying entropy patterns from SD to PR to CR with PD as baseline.
(J) Exemplified violin plots depicting attention head entropy in SD/PD versus CR/PR.
(K) The varying of patterns of tumor evasion signature from SD to PR to CR with PD as baseline.
(L) The varying of patterns of T cell infiltration signature from SD to PR to CR with PD as baseline.
(M) Association between attention head entropy and overall survival on the urothelial carcinoma dataset.
(N) Exemplified survival curves stratified by attention head entropy.

transcriptomes and examined its potential clinical translational relevance. The paradigm underpinning *tGPT* in essence is to predict the occurrence of a given gene with its previous context. We developed *tGPT* on a super large-scale single-cell transcriptome dataset that consists of 22.3 million cells and systematically evaluated its representation learning ability on different single-cell analysis tasks. We noted that *tGPT* was insensitive to batch effect and achieved competitive performance as compared with benchmark tools. The purpose of this study is to verify the validity of this new paradigm in deciphering large-scale transcriptome data, especially at the level of single-cell atlas. In addition, we showed that the pretrained *tGPT* model can be applied to bulk tissue sequencing samples to extract a variety of features exhibiting significant association with genomic alterations and response to immunotherapy treatment.

Artificial intelligence is undergoing a paradigm shift and the pretraining models based on transformer are becoming *de facto* standard in natural language processing and computer vision, achieving state-of-the-art across a wide range of tasks such as natural language understanding, image classification, video and audio recognition.[11] Representative pretraining models include BERT[14] and GPT.[15] The advantage of these pretraining models lie in its ability to assimilate real-world information from super large-scale unlabeled and high-dimensional data. This advantage brings an attractive solution for deciphering single-cell transcriptomes as millions of cells have been sequenced, which exemplified by 22.3 million cells collected in our study. This number is expected to increase exponentially in years ahead. There is no analytical tool that is designed and evaluated on such large volume of data. The high expressivity and scalability of transformer enable *tGPT* to learn rich representation from transcriptomes in a self-supervised manner. The high clustering performance in single-cell cluster delineation is probably attributable to better feature representation learned by *tGPT*. In addition, feature representation from *tGPT* is insensitive to batch effect as the acceptance rate of *kBET* derived from *tGPT* is evenly distributed among the other tools that explicitly used batch information for batch-correction. This is probably because of the use of rankings of top expressing genes rather than actual expression levels by *tGPT*. *tGPT* is quite different from the other integration tools[30,31,39] as the later use the actual expression levels of highly variable genes (HVGs) and the batch information. The independence of *tGPT* on batch information makes it attractive for integration of super large-scale transcriptomes because the batch information is not always available and often neglected by researchers.

The clustering performance in delineating single-cell clusters is robust with respect to the number of top expressing genes used and feature representation extracted from different *tGPT* transformer layers. The clustering metrics obtained from 62 top-expressing genes are comparable to the use of 126 top-expressing genes (Figure S4). This suggested that the rankings of 62 top-expressing genes are sufficient for cell cluster definition. The idea underpinning *tGPT* is to predict the occurrence of a gene in the context of the occurrences of its preceding neighbors. Thistype of pretraining is not directly related to cell clustering. This does not guarantee that feature representation from the last transformer layer could give rise to better clustering as compared with representation from its preceding layers. In our evaluation, the cluster metrics obtained from different transformer layers are comparable and consistently better than the embedding layer (Figure S4). In addition, we observed that cell-type specific genes have high attribution scores albeit only the rankings are used during pretraining. This finding can partially explain why features derived from *tGPT* could lead to high performance in cell clustering. Although this study also uses gene rankings as we did in our previous study,[43] they are theoretically different. *tGPT* builds on autoregressive language modeling[16] whereas the model developed in our previous study used masked language modeling.[14] More importantly, we explored the feature patterns learned by *tGPT* in bulk tissues, which were not investigated in our previous work.

A new finding emerged from our study is that the pretrained *tGPT* model can be applied to bulk tissues. On the *GTEx* dataset, the feature representations of different organs extracted from *tGPT* can divide samples into distinct clusters, aligning with organs. On the *TCGA* dataset, we observed that different cancer types are well separated and cancers of the same origins are more closely related, which is consistent with

previous report.[44] In addition, the feature patterns of TCGA samples exhibited consistent and significant association with genomic alterations. This indicated that rankings of top-expressing genes carry information about alterations in tumor tissues. Meanwhile, the feature patterns derived from *tGPT* are distinctive among patients with different treatment outcomes for immunotherapy. Token together, our finding would facilitate translational research enabled by super large-scale transcriptomes.

We focused two main directions of *tGPT* for future development. First, *tGPT* can be used to generate large-scale reference mapping with the availability of large-scale disease reference datasets and phenotypes. Second, *tGPT* can be further investigated for clinical application such as treatment guiding and prognostic prediction.

Conclusion

In summary, we systematically verified a new, simple and effective analytical paradigm for integration of super large-scale transcriptomes and its implications in clinical translation.

Limitations of the study

First, tGPT uses only the top-expressing genes; therefore, it may miss the information that is specifically represented within the low-expressing genes. Second, tGPT uses gene expression rankings but not actual expression levels. Thus, the fold changes among genes are neglected and this can affect biological interpretation. Third, the language modeling objective function used by tGPT is to predict the gene rankings, which is not directly related to biological issues. Therefore, further study is required to investigate associations between prediction of gene rankings and biological functions.

STAR★METHODS

Detailed methods are provided in the online version of this paper and include the following:

- KEY RESOURCES TABLE
- RESOURCE AVAILABILITY
  - Lead contact
  - Materials availability
  - Data and code availability
- EXPERIMENTAL MODEL AND SUBJECT DETAILS
  - Human Cell Atlas Census of Immune Cells (HCA)
  - Human cell Landscape (HCL)
  - Tabula Mursi
  - The Cancer Genome Atlas (TCGA)
  - Genotype-Tissue Expression Project (GTEx)
- METHOD DETAILS
  - Input preprocessing
  - The architecture of *tGPT*
  - Training scheme
  - Clustering on feature representation from *tGPT*
  - Features derived from self-attention
  - Attention analysis in relation to signaling
  - Diffusion pseudo-time maps construction
  - Benchmark methods
- QUANTIFICATION AND STATISTICAL ANALYSIS
  - Clustering and batch-effect metrics
- ADDITIONAL RESOURCES

SUPPLEMENTAL INFORMATION

Supplemental information can be found online at https://doi.org/10.1016/j.isci.2023.106536.

ACKNOWLEDGMENTS

We are grateful for researchers for their generosity to made their data publicly available. This work was supported by National Key Research and Development Program of China (Grant No. 2021YFC2500400 to K.C.), National Natural Science Foundation of China (Grant No. 32270688 and 31801117 to X.L., 31900471 to M.Y.

and 82073287 to Q.Z.) and Tianjin Municipal Health Commission Foundation (Grant No. RC20027 to Y.L). This work was funded by Tianjin Key Medical Discipline (Specialty) Construction Project (TJYXZDXK-009A).

AUTHOR CONTRIBUTIONS

X.L. and K.C. designed and supervised the study; X.L., H.S., J.L., and J.H. performed data analysis and wrote the manuscript; X.L. developed the model; X.L., H.S., X.S., C.Z., D.W., M.F., J.H., J.L., Y.Y., Y.L., M.Y., W.W., and Q.Z. collected data; H.S., X.L., K.C., and J.Y. revised the manuscript.

DECLARATION OF INTERESTS

The authors declare that they have no conflict of interest.

Received: October 11, 2022
Revised: February 4, 2023
Accepted: March 24, 2023
Published: April 20, 2023

REFERENCES

1. Regev, A., Teichmann, S.A., Lander, E.S., Amit, I., Benoist, C., Birney, E., Bodenmiller, B., Campbell, P., Carninci, P., Clatworthy, M., et al. (2017). The human cell atlas. Elife *6*.

2. Papatheodorou, I., Moreno, P., Manning, J., Fuentes, A.M.-P., George, N., Fexova, S., Fonseca, N.A., Füllgrabe, A., Green, M., Huang, N., et al. (2020). Expression Atlas update: from tissues to single cells. Nucleic Acids Res. *48*, D77–D83.

3. Wilk, A.J., Rustagi, A., Zhao, N.Q., Roque, J., Martínez-Colón, G.J., McKechnie, J.L., Ivison, G.T., Ranganath, T., Vergara, R., Hollis, T., et al. (2020). A single-cell atlas of the peripheral immune response in patients with severe COVID-19. Nat. Med. *26*, 1070–1076.

4. Tabula Muris Consortium; Overall coordination; Logistical coordination; Organ collection and processing; Library preparation and sequencing; Computational data analysis; Cell type annotation; Writing group; Supplemental text writing group; Principal investigators (2018). Single-cell transcriptomics of 20 mouse organs creates a Tabula Muris. Nature *562*, 367–372. https://doi.org/10.1038/s41586-018-0590-4.

5. Han, X., Wang, R., Zhou, Y., Fei, L., Sun, H., Lai, S., Saadatpour, A., Zhou, Z., Chen, H., Ye, F., et al. (2018). Mapping the mouse cell atlas by microwell-seq. Cell *173*, 1307. https://doi.org/10.1016/j.cell.2018.05.012.

6. Tung, P.Y., Blischak, J.D., Hsiao, C.J., Knowles, D.A., Burnett, J.E., Pritchard, J.K., and Gilad, Y. (2017). Batch effects and the effective design of single-cell gene expression studies. Sci. Rep. *7*, 39921. https://doi.org/10.1038/srep39921.

7. Hicks, S.C., Townes, F.W., Teng, M., and Irizarry, R.A. (2018). Missing data and technical variability in single-cell RNA-sequencing experiments. Biostatistics *19*, 562–578. https://doi.org/10.1093/biostatistics/kxx053.

8. Lopez, R., Regier, J., Cole, M.B., Jordan, M.I., and Yosef, N. (2018). Deep generative modeling for single-cell transcriptomics. Nat. Methods *15*, 1053–1058. https://doi.org/10.1038/s41592-018-0229-2.

9. Amodio, M., van Dijk, D., Srinivasan, K., Chen, W.S., Mohsen, H., Moon, K.R., Campbell, A., Zhao, Y., Wang, X., Venkataswamy, M., et al. (2019). Exploring single-cell data with deep multitasking neural networks. Nat. Methods *16*, 1139–1145. https://doi.org/10.1038/s41592-019-0576-7.

10. Simon, L.M., Wang, Y.-Y., and Zhao, Z. (2021). Integration of millions of transcriptomes using batch-aware triplet neural networks. Nat. Mach. Intell. *3*, 705–715.

11. Bommasani, R., Hudson, D.A., Adeli, E., Altman, R., Arora, S., von Arx, S., Bernstein, M.S., Bohg, J., Bosselut, A., and Brunskill, E. (2021). On the opportunities and risks of foundation models. Preprint at arXiv. https://doi.org/10.48550/arXiv:2108.07258.

12. Chen, M., Radford, A., Child, R., Wu, J., Jun, H., Luan, D., and Sutskever, I. (2020). Generative Pretraining from Pixels (PMLR), pp. 1691–1703.

13. Bao, H., Dong, L., and Wei, F. (2021). BEiT: BERT pre-training of image transformers. Preprint at arXiv. https://doi.org/10.48550/arXiv:2106.08254.

14. Devlin, J., Chang, M.-W., Lee, K., and Toutanova, K. (2018). Bert: pre-training of deep bidirectional transformers for language understanding. Preprint at arXiv. https://doi.org/10.48550/arXiv:1810.04805.

15. Radford, A., Narasimhan, K., Salimans, T., and Sutskever, I. (2018). Improving Language Understanding by Generative Pre-training.

16. Brown, T.B., Mann, B., Ryder, N., Subbiah, M., Kaplan, J., Dhariwal, P., Neelakantan, A., Shyam, P., Sastry, G., and Askell, A. (2020). Language models are few-shot learners. Preprint at arXiv. https://doi.org/10.48550/arXiv:2005.14165.

17. Wang, H., Sun, Q., Zhao, W., Qi, L., Gu, Y., Li, P., Zhang, M., Li, Y., Liu, S.L., and Guo, Z. (2015). Individual-level analysis of differential expression of genes and pathways for personalized medicine. Bioinformatics *31*, 62–68. https://doi.org/10.1093/bioinformatics/btu522.

18. Qi, L., Li, T., Shi, G., Wang, J., Li, X., Zhang, S., Chen, L., Qin, Y., Gu, Y., Zhao, W., and Guo, Z. (2017). An individualized gene expression signature for prediction of lung adenocarcinoma metastases. Mol. Oncol. *11*, 1630–1645. https://doi.org/10.1002/1878-0261.12137.

19. Peng, F., Wang, R., Zhang, Y., Zhao, Z., Zhou, W., Chang, Z., Liang, H., Zhao, W., Qi, L., Guo, Z., and Gu, Y. (2017). Differential expression analysis at the individual level reveals a lncRNA prognostic signature for lung adenocarcinoma. Mol. Cancer *16*, 98. https://doi.org/10.1186/s12943-017-0666-z.

20. Peng, F., Zhang, Y., Wang, R., Zhou, W., Zhao, Z., Liang, H., Qi, L., Zhao, W., Wang, H., Wang, C., et al. (2016). Identification of differentially expressed miRNAs in individual breast cancer patient and application in personalized medicine. Oncogenesis *5*, e194. https://doi.org/10.1038/oncsis.2016.4.

21. Liu, P.J., Saleh, M., Pot, E., Goodrich, B., Sepassi, R., Kaiser, L., and Shazeer, N. (2018). Generating wikipedia by summarizing long sequences. Preprint at arXiv. https://doi.org/10.48550/arXiv:1801.10198.

22. Regev, A., Teichmann, S., Rozenblatt-Rosen, O., Stubbington, M., Ardlie, K., Amit, I., Arlotta, P., Bader, G., Benoist, C., and Biton, M. (2018). The human cell atlas white paper. Preprint at arXiv. https://doi.org/10.48550/arXiv.1810.05192.

23. Han, X., Zhou, Z., Fei, L., Sun, H., Wang, R., Chen, Y., Chen, H., Wang, J., Tang, H., Ge, W., et al. (2020). Construction of a human cell landscape at single-cell level. Nature *581*, 303–309. https://doi.org/10.1038/s41586-020-2157-4.

24. Peng, Y.R., Shekhar, K., Yan, W., Herrmann, D., Sappington, A., Bryman, G.S., van Zyl, T., Do, M.T.H., Regev, A., and Sanes, J.R. (2019). Molecular classification and comparative

taxonomics of foveal and peripheral cells in primate retina. Cell *176*, 1222–1237.e22. https://doi.org/10.1016/j.cell.2019.01.004.

25. GTEx Consortium (2018). Erratum: genetic effects on gene expression across human tissues. Nature *553*, 530. https://doi.org/10.1038/nature25160.

26. Thorsson, V., Gibbs, D.L., Brown, S.D., Wolf, D., Bortone, D.S., Ou Yang, T.H., Porta-Pardo, E., Gao, G.F., Plaisier, C.L., Eddy, J.A., et al. (2018). The immune landscape of cancer. Immunity *48*, 812–830.e14. https://doi.org/10.1016/j.immuni.2018.03.023.

27. Johnson, W.E., Li, C., and Rabinovic, A. (2007). Adjusting batch effects in microarray expression data using empirical Bayes methods. Biostatistics *8*, 118–127. https://doi.org/10.1093/biostatistics/kxj037.

28. Haghverdi, L., Lun, A.T.L., Morgan, M.D., and Marioni, J.C. (2018). Batch effects in single-cell RNA-sequencing data are corrected by matching mutual nearest neighbors. Nat. Biotechnol. *36*, 421–427.

29. Korsunsky, I., Millard, N., Fan, J., Slowikowski, K., Zhang, F., Wei, K., Baglaenko, Y., Brenner, M., Loh, P.R., and Raychaudhuri, S. (2019). Fast, sensitive and accurate integration of single-cell data with Harmony. Nat. Methods *16*, 1289–1296. https://doi.org/10.1038/s41592-019-0619-0.

30. Butler, A., Hoffman, P., Smibert, P., Papalexi, E., and Satija, R. (2018). Integrating single-cell transcriptomic data across different conditions, technologies, and species. Nat. Biotechnol. *36*, 411–420. https://doi.org/10.1038/nbt.4096.

31. Zhang, L., Yu, X., Zheng, L., Zhang, Y., Li, Y., Fang, Q., Gao, R., Kang, B., Zhang, Q., Huang, J.Y., et al. (2018). Lineage tracking reveals dynamic relationships of T cells in colorectal cancer. Nature *564*, 268–272. https://doi.org/10.1038/s41586-018-0694-x.

32. Polański, K., Young, M.D., Miao, Z., Meyer, K.B., Teichmann, S.A., and Park, J.-E. (2020). BBKNN: fast batch alignment of single cell transcriptomes. Bioinformatics *36*, 964–965.

33. Hie, B., Bryson, B., and Berger, B. (2019). Efficient integration of heterogeneous single-cell transcriptomes using Scanorama. Nat. Biotechnol. *37*, 685–691.

34. Liu, X., Zhang, F., Hou, Z., Wang, Z., Mian, L., Zhang, J., and Tang, J. (2020). Self-supervised learning: generative or contrastive. Preprint at arXiv. https://doi.org/10.48550/arXiv:2006.08218.

35. Lotfollahi, M., Naghipourfar, M., Luecken, M.D., Khajavi, M., Büttner, M., Wagenstetter, M., Avsec, Ž., Gayoso, A., Yosef, N., Interlandi, M., et al. (2022). Mapping single-cell data to reference atlases by transfer learning. Nat. Biotechnol. *40*, 121–130. https://doi.org/10.1038/s41587-021-01001-7.

36. Wang, D., Hou, S., Zhang, L., Wang, X., Liu, B., and Zhang, Z. (2021). iMAP: integration of multiple single-cell datasets by adversarial paired transfer networks. Genome Biol. *22*, 63. https://doi.org/10.1186/s13059-021-02280-8.

37. Li, X., Wang, K., Lyu, Y., Pan, H., Zhang, J., Stambolian, D., Susztak, K., Reilly, M.P., Hu, G., and Li, M. (2020). Deep learning enables accurate clustering with batch effect removal in single-cell RNA-seq analysis. Nat. Commun. *11*, 2338. https://doi.org/10.1038/s41467-020-15851-3.

38. Büttner, M., Miao, Z., Wolf, F.A., Teichmann, S.A., and Theis, F.J. (2019). A test metric for assessing single-cell RNA-seq batch correction. Nat. Methods *16*, 43–49. https://doi.org/10.1038/s41592-018-0254-1.

39. Wolf, F.A., Angerer, P., and Theis, F.J. (2018). SCANPY: large-scale single-cell gene expression data analysis. Genome Biol. *19*, 15. https://doi.org/10.1186/s13059-017-1382-0.

40. Klimchenko, O., Mori, M., DiStefano, A., Langlois, T., Larbret, F., Lecluse, Y., Feraud, O., Vainchenker, W., Norol, F., and Debili, N. (2009). A common bipotent progenitor generates the erythroid and megakaryocyte lineages in embryonic stem cell–derived primitive hematopoiesis. Blood *114*, 1506–1517.

41. Trinchieri, G. (1989). Biology of natural killer cells. Adv. Immunol. *47*, 187–376.

42. LeBien, T.W., and Tedder, T.F. (2008). B lymphocytes: how they develop and function. Blood. The Journal of the American Society of Hematology *112*, 1570–1580.

43. Shen, H., Shen, X., Feng, M., Wu, D., Zhang, C., Yang, Y., Yang, M., Hu, J., Liu, J., Wang, W., et al. (2022). A universal approach for integrating super large-scale single-cell transcriptomes by exploring gene rankings. Briefings Bioinf. *23*, bbab573. https://doi.org/10.1093/bib/bbab573.

44. Hoadley, K.A., Yau, C., Wolf, D.M., Cherniack, A.D., Tamborero, D., Ng, S., Leiserson, M.D.M., Niu, B., McLellan, M.D., Uzunangelov, V., et al. (2014). Multiplatform analysis of 12 cancer types reveals molecular classification within and across tissues of origin. Cell *158*, 929–944.

45. Mariathasan, S., Turley, S.J., Nickles, D., Castiglioni, A., Yuen, K., Wang, Y., Kadel, E.E., III, Koeppen, H., Astarita, J.L., Cubas, R., et al. (2018). TGFbeta attenuates tumour response to PD-L1 blockade by contributing to exclusion of T cells. Nature *554*, 544–548. https://doi.org/10.1038/nature25501.

46. Zhang, X., Lan, Y., Xu, J., Quan, F., Zhao, E., Deng, C., Luo, T., Xu, L., Liao, G., Yan, M., et al. (2019). CellMarker: a manually curated resource of cell markers in human and mouse. Nucleic Acids Res. *47*, D721–D728. https://doi.org/10.1093/nar/gky900.

47. Lawson, K.A., Sousa, C.M., Zhang, X., Kim, E., Akthar, R., Caumanns, J.J., Yao, Y., Mikolajewicz, N., Ross, C., Brown, K.R., et al. (2020). Functional genomic landscape of cancer-intrinsic evasion of killing by T cells. Nature *586*, 120–126. https://doi.org/10.1038/s41586-020-2746-2.

48. Vaswani, A., Shazeer, N., Parmar, N., Uszkoreit, J., Jones, L., Gomez, A.N., Kaiser, Ł., and Polosukhin, I. (2017). Attention Is All You Need, pp. 5998–6008.

49. Cheng, J., Dong, L., and Lapata, M. (2016). Long short-term memory-networks for machine reading. Preprint at arXiv. https://doi.org/10.48550/arXiv:1601.06733.

50. Traag, V.A., Waltman, L., and van Eck, N.J. (2019). From Louvain to Leiden: guaranteeing well-connected communities. Sci. Rep. *9*, 5233. https://doi.org/10.1038/s41598-019-41695-z.

51. Becht, E., McInnes, L., Healy, J., Dutertre, C.-A., Kwok, I.W.H., Ng, L.G., Ginhoux, F., and Newell, E.W. (2019). Dimensionality reduction for visualizing single-cell data using UMAP. Nat. Biotechnol. *37*, 38–44.

52. Ghader, H., and Monz, C. (2017). What does attention in neural machine translation pay attention to?. Preprint at arXiv. https://doi.org/10.48550/arXiv:1710.03348.

53. Michel, P., Levy, O., and Neubig, G. (2019). Are sixteen heads really better than one?. Preprint at arXiv. https://doi.org/10.48550/arXiv:1905.10650.

54. Vig, J., Madani, A., Varshney, L.R., Xiong, C., Socher, R., and Rajani, N.F. (2020). Bertology meets biology: interpreting attention in protein language models. Preprint at arXiv. https://doi.org/10.48550/arXiv:2006.15222.

55. Schiebinger, G., Shu, J., Tabaka, M., Cleary, B., Subramanian, V., Solomon, A., Gould, J., Liu, S., Lin, S., Berube, P., et al. (2019). Optimal-transport analysis of single-cell gene expression identifies developmental trajectories in reprogramming. Cell *176*, 1517–1943.

56. Reichardt, J., and Bornholdt, S. (2006). Statistical mechanics of community detection. Phys. Rev. *74*, 016110.

57. Malkov, Y.A., and Yashunin, D.A. (2020). Efficient and robust approximate nearest neighbor search using hierarchical navigable small world graphs. IEEE Trans. Pattern Anal. Mach. Intell. *42*, 824–836.

58. Johnson, W.E., Li, C., and Rabinovic, A. (2007). Adjusting batch effects in microarray expression data using empirical Bayes methods. Biostatistics *8*, 118–127.

59. Wołk, K., and Marasek, K. (2015). Enhanced bilingual evaluation understudy. Preprint at arXiv. https://doi.org/10.48550/arXiv:1509.09088.

STAR★METHODS

KEY RESOURCES TABLE

REAGENT or RESOURCE	SOURCE	IDENTIFIER
Deposited data		
Raw and analyzed data	https://data.humancellatlas.org/explore/projects/cc95ff89-2e68-4a08-a234-480eca21ce79?catalog=dcp1	Census of Immune Cells
Raw and analyzed data	https://www.ncbi.nlm.nih.gov/geo/download/?acc=GSE134355&format=file	GSE134355
Raw and analyzed data	https://www.ncbi.nlm.nih.gov/geo/query/acc.cgi?acc=GSE118546; https://www.ncbi.nlm.nih.gov/geo/query/acc.cgi?acc=GSE118852	GSE118480
Raw and analyzed data	https://www.ncbi.nlm.nih.gov/geo/download/?acc=GSE96583	GSE96583
Software and algorithms		
Scanpy (v1.6.0)	(Wolf et al., 2018)[39]	https://github.com/theislab/scanpy
Pegasus (v1.4.3)	(Bo Li el at., 2020)	https://github.com/lilab-bcb/pegasus
scVI(v0.6.8)	(Lopez et al., 2018)[8]	https://github.com/theislab/scvelo
MNN (v1.8.0)	(Laleh Haghverdi et al.,2018)[28]	https://github.com/MarioniLab/MNN2017
Combat (v1.8.0)	(Jean-Philippe Fortin et al.,2017)	https://github.com/Jfortin1/ComBatHarmonization
Harmony (v0.1.6)	(Ilya Korsunsky et al., 2019)[29]	https://github.com/immunogenomics/harmony
Seurat (v3.1.5)	(Butler et al., 2018)[30]	https://satijalab.org/seurat
Scanorama (v1.7.1)	(Brian Hie *el al.*,2019)[33]	https://github.com/brianhie/scanorama
DESC (v2.1.1)	(Xiangjie Li *et at.*, 2020)[37]	https://eleozzr.github.io/desc/
iMAP (v1.0.0)	(Dongfang Wang *et at.*, 2021)[36]	https://github.com/Svvord/iMAP
scArches (v 1.7.0)	(Mohammad Lotfollahi et al., 2021)[35]	https://github.com/theislab/scarches
BBKNN (v 1.7.1)	(Krzysztof Polański et al., 2020)[32]	https://github.com/Teichlab/bbknn
tGPT	(Hongru Shen et al., 2023)	https://github.com/deeplearningplus/tGPT

RESOURCE AVAILABILITY

Lead contact

Further information and requests for resources and materials should be directed to andwill be fulfilled by the lead contact, Xiangchun Li (lixiangchun2014@foxmail.com).

Materials availability

This study did not generate new unique reagents.

Data and code availability

- All the gene expression matrices were downloaded from public databases. The source list of these datasets was provided in the key resources table and Table S1. Source code is available at https://github.com/deeplearningplus/tGPT.
- Any additional information required to reanalyze the data reported in this paper is available from the lead contact upon request.

EXPERIMENTAL MODEL AND SUBJECT DETAILS

We collected the transcriptomes of 22.3 million single-cells (Table S1), 9318 bulk tissue transcriptomes of TCGA cohort from the supplemental data of pan-cancer immune landscape study,[26] 11,688 bulk tissue transcriptomes from *GTEx*database[25] and 298 bulk tissue transcriptomes from the clinical trial study on immunotherapy for urothelial carcinoma.[45] We discarded mitochondrial genes, ribosomal genes and

non-protein coding genes for the single-cell data. Four single-cell and two bulk tissue sequencing datasets are used in downstream evaluation of *tGPT*. Annotated cell labels provided by the original studies are used as the ground truth label (Table S2).

Human Cell Atlas Census of Immune Cells (HCA)

Bone marrow cells (n = 282,588) from 64 healthy donors in *Human Cell Atlas* (*HCA*) project. The data are subjected to 10x sequencing protocol[22] and contained 18 cell types such as hematopoietic stem cells (HSCs), mesenchymal stem cells (MSCs), erythrocytes, megakaryocytes and different kinds of immune cells.

Human cell Landscape (HCL)

HCL dataset includes 586,135 human cells obtained from a Chinese Han population,[23] the dataset encompasses samples of fetal and adult tissue and covered 60 human tissue types, and are subjected to Microwell-seq protocol.

Tabula Mursi

The *Tabula Muris* dataset (n = 54,865) is consisted of single-cells sorted by FACS from Mouse Cell Atlas[4] across 20 different organs subjected to 10x and Smart-seq2 sequencing protocols.

The Cancer Genome Atlas (TCGA)

The *TCGA* dataset is consisted of 9,318 bulk samples with primary cancer and matched normal samples spanning 33 cancer types.

Genotype-Tissue Expression Project (GTEx)

The *GTEx* dataset includes 11,688 bulk samples across 30 organs obtained from healthy donors.

Known marker genes of different cell types are curated from CellMarker database[46]: plasma cell (*MZB1*), DCs and monocytes (*CST3*, *FCER1A*, *IRF7*, *CD14* and *FCGR3A*), megakaryocyte (*PPBP* and *PF4*), B cell (*CD79A*, *CD79B* and *MS4A1*) NK and cytotoxic T cell (*NKG7*, *FGFBP2*, *GNLY*, *GZMA*, *GZMB* and *PRF1*).

Cell state signatures are curated from CellMarker database,[46] including progenitor signaling (*STMN1*, *TUBA1B* and *HIST1H4C*), naïve signaling (*CCR7*, *LEF1* and *SELL*) and cytotoxic signaling (*GZMA*, *CD8A*, *CD8B*, *GZMB*, *PRF1*, *IL2*, *GNLY*, *GAMK*, *IFNG* and *NKG7*).

T cellinfiltration signature is obtained from CellMarker database[46]; it consists of *CD3D*, *CD3E* and *CD8A*.

Tumor evasion signature is curated from the Figure 1 of a previous study.[47]

METHOD DETAILS

Input preprocessing

The input sequence list of top-expressing genes was obtained via descending sorting. The input to *tGPT* was formulated as [<*s*>, G_1, G_2, G_3, …,<*e*>], where G_1, G_2 and G_3 are gene symbols and<*s*>and<*e*>are two special tokens respectively added to the start and end of the input sequence. The input sequence is padded with special token<*pad*>if its length is less than a predefined value. The input sequence list is truncated if its length exceeds the predefined value. We evaluated a length of 64 and 128 in this study. The dictionary used by *tGPT* consists of 20706 protein-coding genes.

The architecture of *tGPT*

Embedding layer transforms the input gene symbols into a real-value matrix that carries the information on gene token embedding and position encoding. The gene token embedding was obtained via an embedding layer (parameterized as W_e) that maps the indices of input genes obtained from the gene symbol dictionary to real-value space. The position encoding (parameterized as W_p) carries information on the sorted gene rankings. For an input sequence $U = \{G_{-k}, \ldots G_{-1}\}$, where k is the width of context window, the embedding layer injects position encoding onto gene token embedding as:

$$h_0 = UW_e + W_p$$

Transformer decoder blocks applies multi-headed masked self-attention over the input embeddings followed by position-wise feed-forward layers, then through a *softmax* layer. *tGPT* use a multi-layer of *transformer decoder*.[21]

$$h_l = \psi(h_{l-1}) \forall i \in [1, n]$$

$$P(U) = \varphi(h_n W_t^T)$$

where ψ is the transformer decoder block and φ is the softmax layer, and W_t is the embedding matrix of the l^{th} decoder block.

Masked Self-Attention is a variant self-attention mechanism.[48] Each attention head adopts the scale dot-product attention to map a query and a set of key-value pairs to an output. The input consists of query and key of dimension d_k, and value of dimensions d_v. Self-attention is calculated as dot products of the query (Q_i) with key (K_i) divided each by $\sqrt{d_k}$ and multiply with value (V_i) after *sofmax* transformed[49]:

$$SelfAttn_i(Q_i, K_i, V_i) = softmax\left(\frac{Q_i K_i^T}{\sqrt{d_k}}\right) V_i$$

Masked self-attention is implemented with the aid of attention mask. It basically always scores the future tokens as 0 so *tGPT* cannot pick from future. The multi-head self-attention is formulated as:

$$MultiHead(Q, K, V) = Concat(SelfAttn_1, ..., SelfAttn_h) W^O$$

where $W^O \in \mathbb{R}^{hd_v \times d_{model}}$ denotes the learned output projection matrix.

Position-wise FeedForward neural network is a layer with fully-connected feed-forward layer. This layer consists of two linear transformations with a *ReLu* activation function in between:

$$FFN(x) = max(0, xW_1 + b_1) W_2 + b_2$$

where W_1 and W_2 are weight matrices and b_1 and b_2 are the bias.

Training scheme

tGPT was pretrained with a batch-size of 64 for 100 epochs. We used Adam with $\beta_1 = 0.9$, $\beta_2 = 0.95$, weight decay of 0.01 and a learning rate of 0.003. The learning rate is warmed up for four epochs, and then decays to 0 following a cosine schedule.[12] *tGPT* was trained with *PyTorch* (version 1.7.1) and *transformers* (version 4.10.0) on NVIDIA DGX A100 with 8 GPUs each with 40 Gb memory.

Clustering on feature representation from *tGPT*

We respectively extracted the feature representations from the embedding layer and 8 different transformer layers. The extracted features were used to construct K-Nearest Neighbors (KNN) graphs for subsequent community detection by Leiden algorithm[50] implemented in *Scanpy* (version 1.8.1). We performed grid-search to identify optimal values of two parameters *n_neighbors* and *resolution* that are the most relevant for clustering. Batch-correction was not applied in clustering. The value of *n_neighbors* examined was ranged from 5 to 100 with step of 5. The value of *resolution* examined was ranged from 0.1 to 2 with step of 0.2. The uniform manifold approximation and projection (UMAP) visualization[51] is used.

Features derived from self-attention

Entropy of the self-attention matrices for a given input sequence is calculated as[52]:

$$Entropy_\alpha(x_i) = -\sum_{j=1}^{i} \alpha_{i,j}(x) \log(\alpha_{i,j}(x)),$$

where α is the self-attention matrix and $\alpha_{i,j}$ is the attention weight between the i^{th} and j^{th} tokens. We averaged the entropy of all cells in a cluster to derive a cluster-level entropy.

Head importance score[53] is defined as the influence of input on head output. It is calculated via gradient backpropagation, formulated as:

$$I_h = \mathbb{E}_{x\sim X}\left|SelfAttn_h(x)^T \frac{\partial \mathcal{L}(x)}{\partial SelfAttn_h(x)}\right|$$

where x is the input sequence and $\mathcal{L}(x)$ is the corresponding loss given the input. I_h is high score while $SelfAttn_h(x)$ is liable to have a large effect on the model.

Token attribution score is defined as the norm of the learned token features (x_i) extracted from *tGPT*, which is defined as:

$$Attribution = \sqrt[2]{x_1^2 + x_2^2 + \ldots + x_N^2}$$

Attention analysis in relation to signaling

We define an attention-based pathway signaling score in a similar way as[54]:

$$p_\alpha(f) = \sum_{x\in X}\sum_{i=1}^{x}\sum_{j=1}^{x} f(i,j)\alpha_{i,j}(x) \Big/ \sum_{x\in X}\sum_{i=1}^{x}\sum_{j=1}^{x} \alpha_{i,j}(x)$$

where $\alpha_{i,j}$ is the attention weight between the i^{th} and j^{th} gene. For a given gene signature, we set $f(i,j) = 1$ if the i^{th} gene or j^{th} gene occurs in that gene set.

Diffusion pseudo-time maps construction

We constructed the diffusion pseudo-time maps using package *Pegasus*[34] (v1.4.3), and the cell trajectory was visualized with force-directed layout embedding (FLE) algorithm.[55] We set δ and $n\delta$ to its default values: δ = 2.0 and $n\delta$ =5,000.

Firstly, we used the features obtained from last transformer decoder blocks to construct affinity matrix of cells $W_{n\times n}$, and the top-k nearest neighbor cells were find by community detection algorithm[56] and the HNSW algorithm,[57] and the formula of affinity matrix is define as:

$$K(x,y) = \left(\frac{2\sigma_x\sigma_y}{\sigma_x^2+\sigma_y^2}\right)^{\frac{1}{2}} \exp\left(-\frac{\|x-y\|^2}{\sigma_x^2+\sigma_y^2}\right) \quad \text{(Equation 1)}$$

$$k'(x,y) = \frac{K(x,y)}{q(x)q(y)} \quad \text{(Equation 2)}$$

$$W(x,y) = \begin{cases} k'(x,y), y\in n(x)/x\in n(x) \\ 0, otherwise \end{cases} \quad \text{(Equation 3)}$$

The Equation 1 represented the distance between cell-x and cell-y, σ_x is the x's local kernel width, x and y are features of last transformer decoder block for cell-x and cell-y. The affinity matrix W was calculated as the density-normalized kernel according to Equation 3.

We then calculated the Markov chain transition matrix P and the symmetric transition matrix Q as the formula:

$$D = diag\left(\sum_y W(x,y)\right)$$

$$P = D^{-1}W, Q = D^{-\frac{1}{2}}WD^{-\frac{1}{2}}$$

The symmetrical matrix Q can be decomposed as UAU^T. Let $\Psi = D^{-\frac{1}{2}}U$. A family with parameter timescale of t for approximated diffusion maps $\{\Psi_t\}_{t \in \mathbb{N} \cup \{\infty\}}$ is defined as:

$$\Psi_t(x_i) = \begin{pmatrix} \lambda_1^t \Psi_1(i) \\ \lambda_2^t \Psi_2(i) \\ \vdots \\ \lambda_{n-1}^t \Psi_{n-1}(i) \end{pmatrix}$$

$$\Psi_t'(x_i) = \sum_{t'=1}^{t} \Psi_{t'}(x_i) = \begin{pmatrix} \lambda_1 \frac{1-\lambda_1^t}{1-\lambda_1} \Psi_1(i) \\ \lambda_2 \frac{1-\lambda_2^t}{1-\lambda_2} \Psi_2(i) \\ \vdots \\ \lambda_{n-1} \frac{1-\lambda_{n-1}^t}{1-\lambda_{n-1}} \Psi_{n-1}(i) \end{pmatrix}$$

Benchmark methods

We also performed single-cell analysis using *Scanpy* (version 1.6.0), *Pegasus* (version 1.4.3) and *scVI* (version 0.13.0). Batch-correction was performed with *MNN* (version 1.8.0),[28] *Combat* (version 1.8.0),[58] *Harmony* (version 0.1.6),[29] *Seurat* (version 3.1.5),[30,31] *Pegasus* (version 1.4.3),[34] *Scanorama* (version 1.7.1),[33] *DESC* (version 2.1.1),[37] *iMAP* (version 1.0.0),[36] *scVI* (version 0.13.0),[8] *scArches* (version 1.7.0),[35] *BBKNN* (version 1.7.1).[32]

Scanpy is a comprehensive toolkit for analyzing single-cell transcriptome. We first filtered out cells with the number of expressing genes <200 or *mitochondrial counts*> 30%. We used the function *scanpy.pp.highly_variable_genes* to selected highly variable genes by setting *max_mean* to 3 and *min_mean* to 0.0125, which are the default values. We then applied clustering pipeline and grid-search to perform single-cell clustering on KNN graph. The UMAP is used for visualizing clustering result.

scVI is a deep generative model for mining the single-cell omics data. We filtered out cells with the number of expressing genes <200 or *mitochondrial counts*> 30%, and selected HVGs with *scanpy.pp.highly_variable_genes* by setting *max_mean* to 3 and *min_mean* to 0.0125. We used the default parameter of *scVI* to extract the 10 latent features. These latent features were used to construct KNN graphs for community detection by Leiden algorithm.[50]

Pegasus is complete single-cell analysis pipline that is efficient on large datasets. We used the recommended parameters: *min_genes* of 500, *max_genes* of 6000, and *percent_mito* of 10. We identified the robust genes with the default *percent_cells* of 0.05. Single-cell clustering was performed on KNN graph followed by Leiden algorithm[50] for community detection.

QUANTIFICATION AND STATISTICAL ANALYSIS

Clustering and batch-effect metrics

We used Adjusted Rand Index (*ARI*), Normalized Mutual information (*NMI*) and Fowlkes-Mallows Index (*FMI*) to measure clustering performance. We used the *kBET* acceptance rate[38] as a measurement of batch-effect. The clustering metrics of *ARI*, *NMI* and *FMI* were calculated with sklearn (version 0.21.2). *kBET* acceptance rate is computed with *Pegasus* (version 1.4.3).

ARI is calculated based on the contingency table summarizing the truth labels and clustering, and the rows and columns represent truth and clustering labels in the contingency table, respectively. The formula is as follows:

$$ARI = \frac{\sum_{ij}\binom{n_{ij}}{2} - \left[\sum_i \binom{a_i}{2} \sum_j \binom{a_j}{2}\right] \Big/ \binom{n}{2}}{\frac{1}{2}\left[\sum_i \binom{a_i}{2} + \sum_j \binom{a_j}{2}\right] - \left[\sum_i \binom{a_i}{2} \sum_j \binom{a_j}{2}\right] \Big/ \binom{n}{2}}$$

where n_{ij} denoted the numbers of cell in common between clustering labels and truth labels, a_i the sum of i^{th} row and a_j the sum of j^{th} column of the contingency table.

NMI is also used to measure the similarity between the clustering labels and actual labels. We assumed that the clustering labels and actual labels of N cells are U and V, and the entropy of U and V is as the following formula:

$$H(U) = -\sum_{i=1}^{|U|} P(i)\log(P(i))$$

$$H(V) = -\sum_{j=1}^{|V|} P'(j)\log(P'(j))$$

where $p(i) = |U_i|/N$ is the probability that a cell picked at random from U falls into U_i, $p'(j) = |V_j|/N$ is the probability that a cell picked at random from V falls into V_j. We then calculated the mutual information (MI) between U and V, and normalized the mutual information:

$$MI(U,V) = \sum_{i=1}^{|U|}\sum_{j=1}^{|V|} P(i,j)\log\left(\frac{P(i,j)}{P(i)P'(j)}\right)$$

$$NMI(U,V) = \frac{MI(U,V)}{\sqrt{H(U)H(V)}}$$

where $p(i,j) = |U_i \cap V_j|/N$ is the probability that a cell picked at random falls into classes U_i and V_j.

Fowlkes-Mallows Index (FMI) is used to measure the consistency between clustering results and real category, and the range of index is from 0 to 1. The *FMI* metric is denfined as the geometric mean between of the precision and recall:

$$FMI = \frac{TP}{\sqrt{(TP+FP)(TP+FN)}}$$

where *TP* is true positive, FP false positive, FN false negiative.

kBET acceptance rate is a measurement of batch effect. We assumed that the dataset of cells with batches of m, and there are n_j cells in batch j. The batch mixing frequency denotes as:

$$f = (f_1, \cdots, f_m)$$

where $f_j = \frac{n_j}{N}$. Then, we calculated the number of neighbors of cell-i belonging to batch j is n_{ji}^k. Its χ^2 test statistic and p-value with degrees of (m-1) are defined as follows:

$$k_i^k = \sum_{j=1}^{m} \frac{\left(n_{ji}^k - f_j \cdot k\right)^2}{f_j \cdot k}$$

$$p_i^k = 1 - F_{m-1}\left(k_i^k\right)$$

where $F_{m-1}(x)$ represents the cumulated density function. The *kBET* acceptance rate is defined as the percentage of cells that accept the null hypothesis at significance level α as follows:

$$kBET - rate = \frac{\sum_{i=1}^{N} I\left(p_i^k \geq \alpha\right)}{N} \times 100\%,$$

I(x) is the indicator function where *I(x)* = 1 if *x*> 0 otherwise *I(x)* = 0. We used *Pegasus* (v1.4.3) to calculate the *kBET* acceptance rate by setting K and α to 5 and 0.01, respectively.

Bilingual Evaluation Understudy (***BLEU***) is an algorithm for evaluating match variable length phrases between output and the reference sequence.[59] The basic metric requires the calculation of a brevity penalty P_B as:

$$P_B = \begin{cases} 1, c > r \\ e^{(1-r/c)}, c \leq r \end{cases}$$

Where r is the length of the reference sequence, and the length of predicted sentence is c.

BLEU score is calculated as:

$$\text{BLEU} = P_B \exp\left(\sum_{n=0}^{N} w_n \log p_n\right)$$

w_n are the positive weights summing to one. p_n is the n-gram precision and it is calculated using n-grames with a maximum length of N.

ADDITIONAL RESOURCES

This study did not generate additional data.